Ocean Engineering 314 (2024) 119674

Contents lists available at ScienceDirect

Ocean Engineering

journal homepage: www.elsevier.com/locate/oceaneng

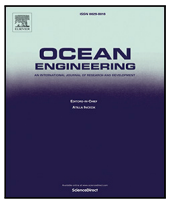

Research paper

Numerical assessment of ship anchor penetration depth in Baltic Sea Sand: Implications for subsea cable burial

D.A. Dao *, J. Grabe

Institute of Geotechnical Engineering and Construction Management, Hamburg University of Technology, Harburger Schloßstr. 36, Hamburg, 21709, Hamburg, Germany

ARTICLE INFO

Keywords:
Subsea cables
Burial depth
Anchor penetration
Baltic sea
Coupled Euler–Lagrange Method (CEL)

ABSTRACT

As renewable energy demand increases, protecting subsea cables from ship anchor damage has become essential. This research comprises numerical simulations of the anchor penetration process in Baltic Sea sand (for an AC-14, a Hall and a Spek anchor). We apply a coupled Eulerian–Lagrangian (CEL) framework and a hypoplasticity constitutive model to analyze the influence of different anchor characteristics on penetration depth and seabed stress distributions. We conducted investigations under high velocities ($v \geq 1$ m/s) with focus on inertial effects only. Furthermore, this study introduces stress circles to visualize a simplified anchor-induced spatial stress distribution in the seabed. Findings show that heavier anchors and slower drag velocities generally result in deeper anchor penetrations. Fluke geometry significantly affects penetration depth, with pointed designs penetrating more deeply. The observed trends align with previous results from centrifuge tests and numerical modeling of ship anchors. This research improves understanding of soil–structure interaction in maritime environments, offering insights for the protection of subsea installations in the Baltic Sea and similar regions.

1. Introduction

The shift to renewable energy is accelerating, growing the need for adequate transportation and storage infrastructure for offshore-generated energy (O'Shaughnessy et al., 2021). Numerous offshore infrastructure projects, including submarine cables in the Baltic Sea, have been planned to support this transition and ensure international energy supply (50Hertz Transmission GmbH, 2024). Protecting these cables against external hazards such as anchor drops and dragging is crucial for their reliability and longevity (Attwood, 2000; Dinmohammadi et al., 2019). Consequently, determining the optimal burial depth for subsea cables and the penetration depth of ship anchors is critical. Traditionally, the burial depth of subsea cables is determined using empirical and statistical methods accounting for factors such as anchor penetration depth, thermal effects induced by the cable, fishing gear, water depth, wave height and seabed conditions (Allan, 1999; Mole et al., 1997; Jongergouw, 2001; Trust, 2015b,a). The penetration depth of ship anchors is estimated using empirical methodologies and numerical simulations, considering variables such as anchor geometry, fluke opening angles, water depth and soil properties (Watson et al., 2022; Lee et al., 2022; Gao et al., 2016; Zhu et al., 2019; Dao and Grabe, 2022; Grabe et al., 2015; Grabe and Wu, 2016). While comprehensive data are available for regions like the North Sea, there is limited data for the Baltic Sea (Bjerrum, 1973; de Kuiter and Beringen, 1979; Andresen et al., 1979; Byrne et al., 2018; Jostad et al., 2020; Jensen and Kellezi, 2023). This leads stakeholders to rely on data from other regions despite the seabed variation in its genesis and therefore its composition, its grain size and corresponding mechanical behavior depending on the body of water (Randolph and Gourvenec, 2017; Atkinson, 2017). Thus, the purpose of this study is to contribute towards ensuring safe and reliable development within the Baltic Sea area. This study represents an inaugural effort in investigating various anchor types, specifically the AC-14, Hall, and Spek anchors, in a Baltic Sea sand environment.

The main objectives of this research are to investigate the penetration depths of different anchor types and explore the factors influencing depth, and subsequently derive implications for the optimal burial depths and design of subsea cables. To accomplish these objectives, this study leverages the Coupled Euler–Lagrange (CEL) approach to simulate the anchor penetration process. The results of this study provide insights for offshore operators, aiding in the design and protection of submarine infrastructure.

* Corresponding author.
E-mail address: duy.anh.dao@tuhh.de (D.A. Dao).

https://doi.org/10.1016/j.oceaneng.2024.119674
Received 6 May 2024; Received in revised form 27 October 2024; Accepted 28 October 2024
Available online 14 November 2024

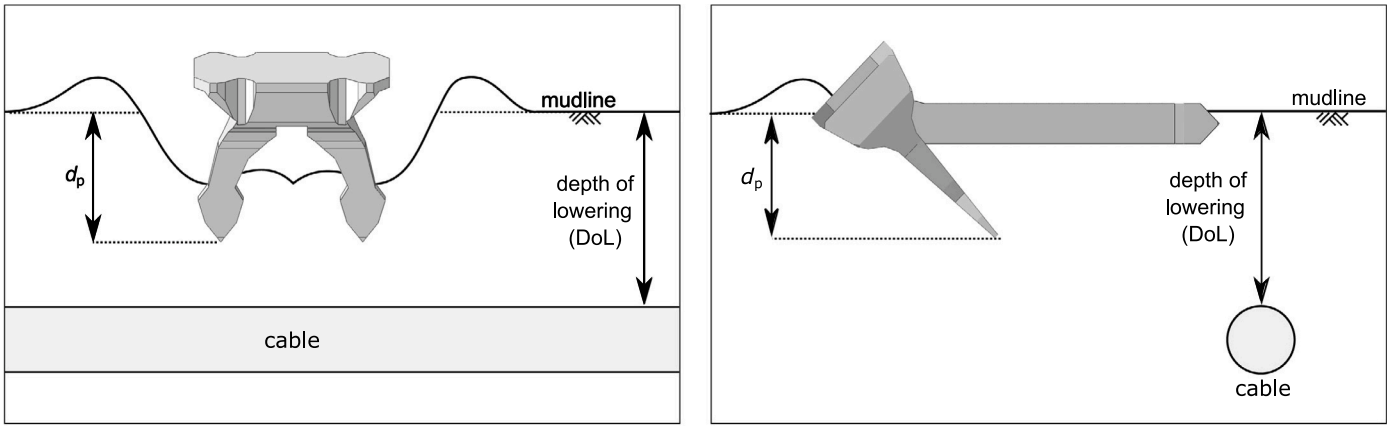

Fig. 1. Front (left) and side (right) view of a penetrating ship anchor and definition of the depth of lowering DoL, according to DNV (2021).

2. Theoretical background

2.1. Assessing the cable burial depth

Identifying the minimal burial depth, also defined as the depth of lowering (DoL), is essential to ensure the resilience and reliability of offshore cable networks. It is defined as the vertical distance between the top of the cable and the undisturbed mean seabed level (mudline), as shown in Fig. 1. Multiple factors, including thermal effects, electromagnetic effects, and mechanical loads, influence the DoL for subsea cables. Mechanical loads present as the most crucial factor for consideration and include trawling, and anchoring. These factors form the critical inputs for the analytical and statistical methods employed to determine the required burial depth.

Recent studies by Hutchison et al. (2021) and Lux et al. (2019) have measured thermal and electromagnetic fields around subsea cables to develop analytical methods capable of deriving the DoL. Legislative bodies such as Germany's Federal Maritime and Hydrographic Agency have introduced related environmental protection standards, such as the 2K-criterion. This directive restricts the permissible increase in sediment temperature to 2 Kelvin at a depth of 0.2 m below the seabed surface, thereby mitigating potential adverse effects of cable heating on marine ecosystems and benthic communities (BSH, 2020).

Established in the 1990s, the Burial Protection Index (BPI) served as a guide to define protective measures for submarine fiber optic cables across diverse seabed conditions. However, the BPI approach is limited to specific anchor sizes, and often overestimates the required protection from fishing gear. In response to these limitations, offshore industries have shifted to more risk-based approaches. The Offshore Wind Accelerator (OWA), an industrial initiative under the Carbon Trust, created the Cable Burial Risk Assessment (CBRA) method to define the optimal and minimum burial depth. This method is recommended by standards such as the DNV-ST-0359 and is applicable to the subsea cable at any point in its life cycle (DNV, 2021). The CBRA approach considers potential risks such as anchor strikes and evolves based on updated site survey data (Trust, 2015b). This approach requires the input of the maximum anchor penetration depth, however the procedure to determine this depth remains undefined. Analytical solutions, as proposed by Neubecker and Randolph (1996a,b,c) and Aubeny and Chi (2010), are well-recognized but appear to overestimate the penetration when compared to field data (Trust, 2015a). Such discrepancies may arise from limitations in accurately determining the soil properties and penetration depth on site during field tests. They may also result from neglecting spatial effects and the use of oversimplified soil constitutive models in the theoretical approaches, as discussed by Dao et al. (2023). When examining physical tests under controlled conditions and 100g, the penetration depths observed are very similar to those predicted by analytical solutions (Sharif et al., 2023; Moore et al., 2021), which likely provide limits on possible penetration depths. Consequently, integrating not only field tests but also physical and validated numerical models for the anchor penetration depth can offer greater reliability and more refined evaluations of the DoL (Trust, 2015a).

2.2. Field tests analyzing anchor penetration depth

Vryhof Anchors (2018) presents a series of field tests conducted at various locations. However, the anchors tested were all permanent anchors used for station-keeping of floating platforms. Luger and Harkes (2013) and BAW (2012) conducted comprehensive field tests that are publicly accessible and were conducted in the North Sea using Side Scan Sonar (SSS) and Sediment Echo Sounder (SES) to analyze the penetration depth of anchors in North Sea seabed. Surface measurements were conducted using SSS both before, and after anchor drops to determine anchor penetration depth. SSS, an area-based procedure, is able to record seafloor surface structures and textures but lacks depth accuracy, making it most applicable as a preliminary step for subsequent SES measurements. The SES, capable of penetrating the seabed, was primarily employed to detect disturbances in the sediment layers, specifically the change of density. SES, operating along a profile line, sends high-frequency acoustic signals to capture sound reflections from the seabed layers. These field tests are referenced by industry standards and guidelines (Trust, 2015a). The specific anchors assessed during these tests were a high holding power (HHP) AC-14 anchor, weighing 8.3 t, and an 11.5 t Hall anchor, both corresponding to a 294 m long container ship with a carrying capacity of 80,000 DWT. Detailed site investigation data for these locations are not freely available due to third-party ownership. Luger and Harkes (2013) report that the relative densities of the first 3 m of sediment were determined from CPT results which typically encounter difficulties in accurately determining such parameters.

The US Naval Civil Engineering Laboratory (1982) conducted a field study in which various anchors were dragged to evaluate their holding capacity and position during dragging. Water pressure sensors were used to measure the pressure at the depth of the fluke to derive the final anchor penetration depth. The study reported anchor depths across various soil conditions at different sites. However, the absence of detailed soil properties makes it difficult to determine the specific conditions under which these depths were achieved and to predict similar outcomes at other locations.

Overall, field tests evaluating anchor penetration are scarce and do not specifically exist for the Baltic Sea.

2.3. Centrifuge tests

Neubecker and Randolph (1996b) and O'Neill and Randolph (2001) executed centrifuge tests in sand and clay. However, the models they used were drag anchors for floating offshore structures. Moore et al. (2021) conducted a centrifuge study to directly measure the penetration depth of an AC-14 anchor at different g-levels in sand immediately after the drag test, rather than deriving it from sensor data. Their findings demonstrated that penetration depth increases with fluke length, indicating a linear relationship between anchor size and penetration depth. Based on these results, they provided recommendations for cable burial depth that account for anchor size and introduced correlations to anchor mass and ship mass. When compared to previous findings, there is a trend of penetration depth decreasing with increasing relative density. Sharif et al. (2023) investigated the penetration behavior of an AC-14 anchor at prototype scale (8.5 t) in sand, focusing on the impact of relative density. Their study confirmed the significance of soil density, showing that the anchor penetrates more deeply in very loose sands than predicted by previous analytical solutions and guidelines.

2.4. Analytical predictions for anchor penetration

The number of existing analytical solutions for determining the trajectory of anchors is limited, specifically ship anchors. However, drag embedment anchors (DEAs) function similarly to ship anchors by mobilizing resistance as they are dragged through the seabed. The analytical models presented by Neubecker and Randolph (1996a), Thorne (1998), and Dahlberg (1998) utilize the Limit Equilibrium Analysis Method to predict the trajectory and bearing capacity of DEAs in clay. Models by Neubecker and Randolph (1996b,c) apply this method to sand environments. These models address the typical loading conditions on DEAs, which include combined normal, tangential, and moment forces. The fundamental analysis is based on principles initially proposed by Murff (1994) for shallow foundations, which were later adapted and expanded by O'Neill et al. (2003). Further refinements by Aubeny and Chi (2010) and Aubeny et al. (2011) have been integrated into international standards, such as those published by the American Bureau of Shipping (2018). The implementation and a detailed examination of the latter are provided in Dao et al. (2024).

2.5. Numerical anchor penetration in sand

A majority of existing research on anchor structure dragging has been conducted within the context of offshore infrastructure, such as the anchor installation of floating platforms, which are similar to ship anchors in function (Peccin Da Silva, 2021; Maitra et al., 2022; Dao et al., 2022; Dao and Dicke, 2024). The CEL method is often applied to analyze the behavior of anchors in soil in these studies. Since this method is able to simulate large deformation problems. It can provide valuable insights into the performance of different anchor types in sandy environments and the risks associated with subsea cable burial due to anchoring activities. It has been applied and validated in numerous geotechnical offshore applications, as shown in Stapelfeldt et al. (2020) and Bienen et al. (2021). The following summary presents the findings on ship anchor penetration derived from CEL simulations.

Table 1 provides a summarized overview of penetration depths from physical tests and numerical simulations. The data presented comprises solely anchors within comparable weight classes and their interactions with sandy seabed conditions.

Although Zhu et al. (2019) and Gao et al. (2016) conducted simulations with Hall anchors of various masses, they only considered vertical penetration, i.e., the anchoring of a ship from a stationary position. Grabe et al. (2015) investigated the penetration behavior of a dragged AC-14 anchor (8.5 t) in sand under varying soil densities, comparing the results with field tests. Based on these findings, they introduced an empirical approach to determine the maximum penetration depth. Osthoff et al. (2017) conducted a numerical case study on an AC-14 anchor (8.3 t) in North Sea sand to investigate its interaction with an embedded steel body, showing that damage can occur even without direct contact due to additionally induced stress. Factors influencing penetration depth included the soil density and the dragging velocity. Dense sand resulted in lower anchor penetration depths and caused a constant alternation between penetration and resurfacing of the anchor over the soil. In some cases, the anchor did not penetrate the soil at all. In addition, lower drag velocities resulted in greater penetration depths.

3. Numerical modeling methodology

In this study, simulations are performed using the finite element method (FEM) with direct explicit time integration in Abaqus/Explicit 2020. The size of the critical time step size Δt_{crit} results from the quotient of the characteristic element length L and the current dilatory wave velocity c_{d} in the element, as shown in Eq. (1).

$$\Delta t_{\text{crit}} = \frac{L_{\text{e}}}{c_{\text{d}}} \quad \text{with} \quad c_{\text{d}} = \sqrt{\frac{E}{\rho}} \tag{1}$$

Here, E represents the modulus of elasticity and ρ the density of the material. By keeping Δt_{crit}, it is ensured that waves in the model do not move through more than one one element per time step. Thus, Δt_{crit} is determined by the finite element with the largest stiffness or the smallest element length. As a result, in geotechnical simulations, stiffer components made of concrete or steel usually dominate the critical time step and thus the calculation time. The formulation by rigid bodies avoids this dominance, since these are not deformable and thus are excluded from determining the critical time step (Dassault Systèmes, 2018).

3.1. The coupled Euler–Lagrange method

The coupled Euler–Lagrange (CEL) approach is employed in this study to address the challenges associated with large soil deformations, which can lead to significant element distortions in the classical FEM with the Lagrange approach and potentially cause the termination of simulations. In this study, the CEL approach is applied to investigate the penetration depth of anchors under drained conditions in the seabed, without considering the dissipation of pore water pressure. The CEL method discretizes structural elements using Lagrangian elements, while the soil is modeled with Eulerian elements. Both descriptions are compared in Fig. 2. In the Lagrangian description, the computational grid is bound to the solid body, deforming with the solid. Each grid point is assigned to a single material point, facilitating the modeling of materials with time-dependent behavior and maintaining a clearly defined solid edge. The motion of the continuum is expressed as a function of material coordinates and time, resulting in an exact surface description but potentially leading to mesh distortions during large deformations.

The Eulerian approach is employed to describe the continuum's motion as a function of spatial coordinates and time. The material can move freely within the Eulerian domain, with the FE mesh serving as a reference mesh that is reset at each simulation timestep. This approach effectively limits the risk of mesh distortions to exceptional cases. However, the properties of the elements are defined by the filling degree of one or more materials, which can result in inaccuracies concerning surface definition and element stiffness. As such, the discretization must be carefully selected. Additionally, a void area must be defined to allow material to uplift. This void possesses neither mass nor stiffness. By utilizing the Eulerian description, a spatially fixed mesh is achieved, allowing the moving and deforming material to flow through the mesh, thereby preventing mesh distortions and ensuring a stable simulation environment.

Table 1
Maximum anchor penetration depths in sand from various sources.

Anchor type	Mass (t)	Relative density I_d (–)	Loading mechanism	Penetration depth (m)	Method	Location	Source
AC-14	8.3	0.15 to 0.35[a]	Drag	0.88	Field test	North Sea	Luger and Harkes (2013)
Hall	11.5	0.15 to 0.35[a]	Drag	0.69	Field test	North Sea	Luger and Harkes (2013)
AC-14	14.4	0.50	Drag	2.58	Centrifuge test	–	Moore et al. (2021)
AC-14	8.5	0.55	Drag	1.10	Centrifuge test	–	Sharif et al. (2023)
Hall	12.5	0.15 to 0.35[a]	Drop	1.60	Numerical	–	Zhu et al. (2019)
AC-14	8.5	0.15	Drag	1.82	Numerical	North Sea	Grabe et al. (2015)
AC-14	8.3	0.50	Drag	0.70	Numerical	North Sea	Osthoff et al. (2017)

[a] Based on given relative density classification.

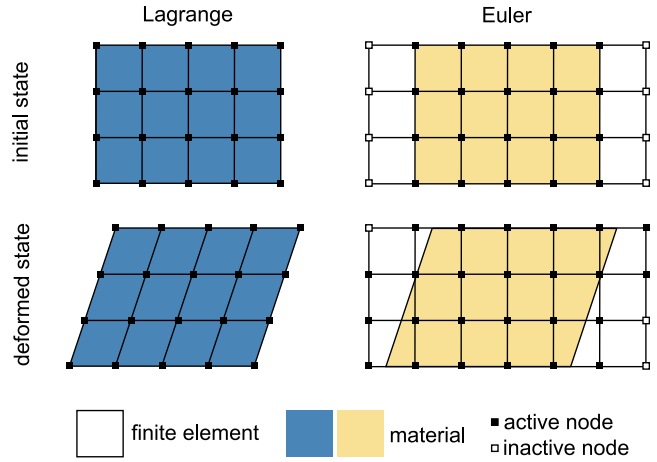

Fig. 2. Deformation of the computational grid with the material (Lagrangian approach, left) and movement of the material through a stationary computational grid (Eulerian approach, right).

Table 2
Depth and relative density of sand layers according to DIN 14688-2 (2020).

Depth range (m)	Soil type	Classification	Relative density[a] I_d (–)
−16.5 to −18.8	fS	Medium dense	0.35 to 0.65
−18.8 to −20.6	fS, u′	Dense	0.65 to 0.85
−20.6 to −21.4	fS, u′	Medium dense	0.35 to 0.65
−21.4 to −22.4	fS, u′	Dense to very dense	0.65 to 1.00

[a] Based on given relative density classification.

In the CEL simulation, both approaches are combined, as presented in Fig. 3. Here, the interaction of the materials or discretization approaches is implemented by a contact algorithm. For the simulations performed here, the penalty contact implemented in Abaqus is used. In case of contact, the structural surface prevents large overlaps of the material boundaries (Dassault Systèmes, 2018).

In application of component penetration, the structure is discretized as a Lagrangian region. The structure can penetrate the Eulerian region and displace the soil in the process. The principle of the CEL method with respect to penetration processes is shown in Fig. 3.

3.2. Modeling of Baltic Sea sand

The sand sample used for this study was collected by vibratory core sampling at the location corresponding to Fig. 4 at a water depth of 16.5 m (MSL). The area surrounding the sand extraction point is part of the Falster-Rügen Sand Plateau (Dao and Banduch, 2023). This flat region consists predominantly of fine sands with varying densities. The relative density of the investigated soil was estimated based on core descriptions in accordance with DIN 14688-2 (2020). Table 2 presents the different layers of the soil sample.

Fig. 5 shows the grain size distribution for this particular Baltic Sea sand sample. The majority of the grains are smaller than 0.2 mm in size. The sharp increase in the curve around this value, along with a uniformity coefficient U of 1.875, indicates that the sediment is well-graded.

In order to simulate the penetration of an anchor into the seabed realistically, the deformation behavior of the soil must be accurately mathematically formulated for an FE analysis using a stress–strain model. This requires considering the pressure and density-dependent stiffness, shear strength, and dilatancy of the soil. The hypoplastic model according to von Wolffersdorff (1996) combined with the extension of the intergranular strain by Niemunis and Herle (1997) meets these requirements for coarse-grained soils. The hypoplastic model with intergranular strain is freely available as a Fortran user routine on SoilModels.com (2024), along with a documentation for implementing it in FEM programs such as Abaqus. It uses a singular non-linear tensorial equation to represent the soil's state, correlating the stress rate $\overset{\circ}{\mathrm{T}}$ with the deformation rate D:

$$\overset{\circ}{\mathrm{T}} = \mathcal{M}(\mathrm{T}, e) : \mathrm{D}. \tag{2}$$

The fourth-order stiffness tensor $\mathcal{M}$ is a function of the stress T and the void ratio e. Admissible void ratios are limited by e_i, e_c and e_d. The three distinct void ratios decrease with increasing mean pressure (trace of T or $3p_s$) and reaching their limit values e_{i0}, e_{c0} and e_{d0} at vanishing mean pressure, as described by following relationship proposed by Bauer (1996). This function includes the granulate hardness h_s and the exponent n.

$$\frac{e_i}{e_{i0}} = \frac{e_c}{e_{c0}} = \frac{e_d}{e_{d0}} = \exp\left[\left(\frac{-\mathrm{trace}(\mathrm{T})}{h_s}\right)^n\right] \tag{3}$$

Laboratory tests were conducted to determine the constitutive parameters (Dao and Banduch, 2023). In oedometer tests, the void ratio e is determined as a function of stress. These tests are used to determine the granulate hardness h_s and the exponent n. Here, h_s is the density-independent parameter of compression and is influenced by the mineral, grain shape and size distribution, among other factors. The parameter n influences the pressure-dependent compression value and depends on the average grain size and the non-uniformity number of the soil particles. To determine the granulate hardness h_s, a one-dimensional compression (oedometer) test is performed on a medium dense sample (I_d = 0.47). The Eq. (3) is used applying a void ratio at zero pressure. The value of h_s is then determined by fitting this equation to the experimental compression data, ensuring no grain crushing within the pressure range being considered. The exponent n accounts for the pressure sensitivity of the soil skeleton and influences how the incremental stiffness increases with pressure. The compression indices C_1 and C_2 at two different pressures p_{s1} and p_{s2} and corresponding void ratios e_1 and e_2 are used to determine n. The value of n is calculated from the following relationship:

$$n = \frac{\ln(e_1 C_2 / e_2 C_1)}{\ln(p_{s2}/p_{s1})} \tag{4}$$

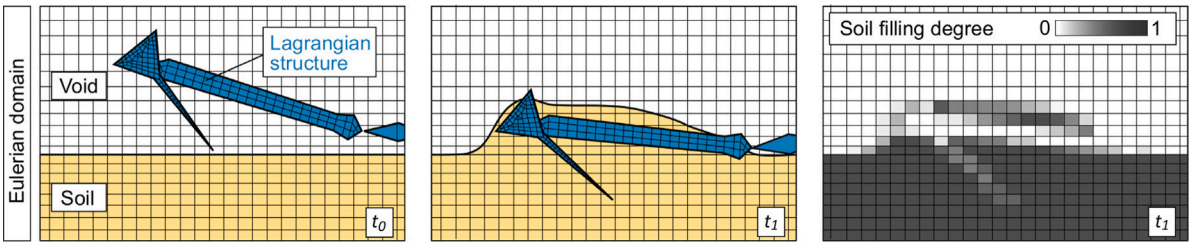

Fig. 3. Schematic 2D representation of the anchor penetration process using the CEL method, showing the initial state (left) and the following state (middle) and the corresponding soil filling degree in correspondence with the resulting soil deformation (right).

Table 3
Hypoplastic parameters for Baltic Sea sand.

Parameter	Value	Unit	Description
ρ	1.9	t/m^3	Density
φ_c	33.58	°	Critical state friction angle
h_s	924.9	MPa	Granulate hardness
n	0.343	–	Pressure-sensitivity exponent
e_{d0}	0.648	–	Minimum void ratio at zero pressure
e_{c0}	1.059	–	Critical state void ratio at zero pressure
e_{i0}	1.218	–	Maximum void ratio at zero pressure
α	0.094	–	Exponent for density dependence of the peak friction angle
β	1.03	–	Exponent for density dependence of the stiffness modulus
m_T	1.87	–	Stiffness increase factor
m_R	3.33	–	Stiffness increase factor
R_{max}	5.82×10^{-6}	–	Maximum intergranular strain
β_χ	0.975	–	Exponent for intergranular strain development
χ	4.01	–	Stiffness degradation exponent

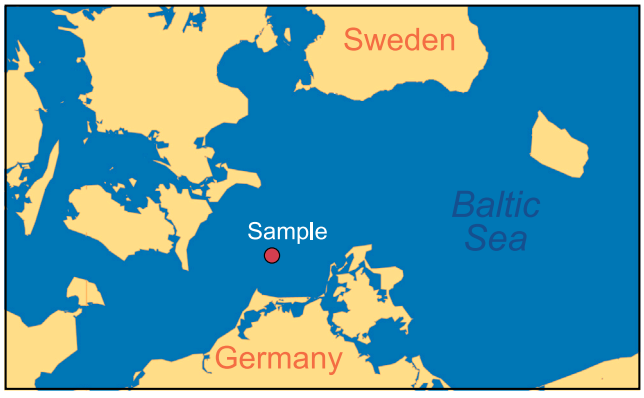

Fig. 4. Soil sample collection point of the Baltic Sea sand.

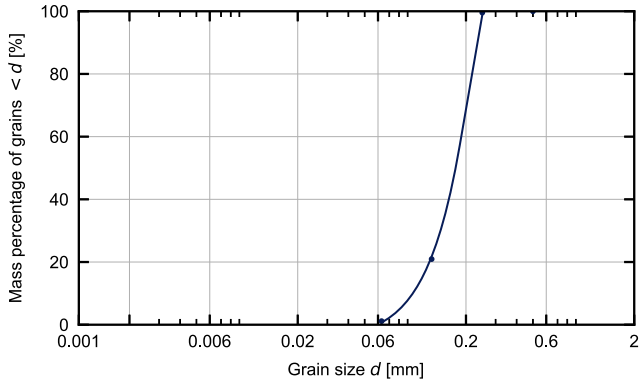

Fig. 5. Grain size distribution of Baltic Sea sand.

This equation derives from the slope of the compression curve in a logarithmic plot and reflects the curvature of the compression curve. Using the test to determine the lowest and highest relative density according to DIN 18126 (2022), the void ratios for e_{d0} and e_{c0} are measured, from which e_{i0} is estimated. Here, e_{d0} corresponds approximately to the minimum void ratio e_{min} and e_{c0} corresponds approximately to the maximum void ratio e_{max}. The void ratio e_{i0} is estimated by 1.15 to 1.20 times e_{max} (Herle and Gudehus, 1999).

For a loose ($I_d = 0.27$) and a dense ($I_d = 1.00$) sample, one triaxial test is performed on each sample to determine the exponents α and β. Both are constant parameters that are used to calculate the stiffness change. The parameter α describes the influence of the density dependence of the peak friction angle φ_p of coarse-grained soils. Here, β is the factor for the stress rate at constant deformation rate and constant mean pressure, which increases with increasing density. The critical state friction angle φ_c is determined from the angle of repose. An alternative method for determining the critical state angle is provided by Santamarina and Cho (2001). Furthermore, the authors note that although the effects of confining pressure on soil dilation are considered, there may be some discrepancies due to the absence of a specific peak friction angle determined for very low confining pressures (Giampa and Bradshaw, 2018).

The five parameters of the extended small strain stiffness model are determined by means of three triaxial tests under different strain history specifications. From these, the values for the parameters R_{max}, m_T and m_R are determined. The material constant R_{max} is independent of pressure and gives the maximum value for the intergranular strains. The parameters m_T and m_R describe the stiffness when the strain direction changes. A more detailed description for the determination of all parameters is given by Herle and Gudehus (1999).

Table 3 shows the determined material properties for the sand.

In Fig. 6, the results of a series of three CU triaxial tests from laboratory tests ($I_d = 0.96, 0.98, 1.03$) and FE analyses with the hypoplastic model are shown to validate the calibration of the constitutive parameters.

The numerical prediction shows a gradual increase in stress with strain but at a lower rate than the experimental data. This underestimation of stress for a given strain results in a conservative estimate

Table 4
Dimensions of the AC-14, Hall and Spek anchor models.

Anchor type	Mass (kg)	A (mm)	B (mm)	C (mm)	D (mm)	E (mm)	F (mm)	G (mm)	H (mm)	θ_{fs} (°)
AC-14	675	1398	1254	387	236	828	654	167	215	35
AC-14	8325	3221	2890	893	556	1961	1548	400	540	35
Hall	11 100	3638	2803	1297	433	1970	1970	437	600	45
Spek	29 000	4621	3438	1494	748	2494	2494	748	820	40

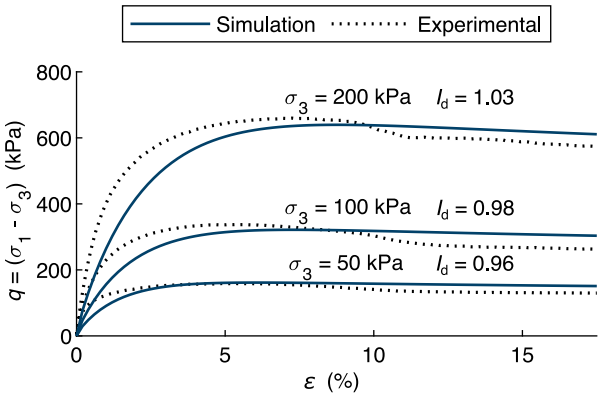

Fig. 6. Comparison of CU triaxial tests ($I_d = 0.96, 0.98, 1.03$) for Baltic Sea sand from laboratory tests and numerical simulations.

of the soil's stiffness. At peak stress, the numerical predictions slightly underestimate the peak in some cases, leading to safer assumptions as well. In the post-peak region, the numerical model's predictions show a more gradual decline in stress compared to the sharper drop observed in the experimental results, with overall differences in the post-peak region being less than 10 %. Overall, the numerical calculations generally show good agreement with the laboratory test for the given sand, thus ensuring safe predictions. Adjusting the constitutive parameters to better fit the initial stiffness resulted in an increase in the overall error. Therefore, we decided to proceed with the current parameter set, accepting this limitation.

3.3. Anchor models

For the analyses, commercially available anchors, the AC-14 weighing 8325 kg and the Hall weighing 11 100 kg, were selected due to their similar weight class to the anchors discussed in Section 2.2. Additionally, to derive conclusions on the influence of weight, an extremely light anchor, the AC-14 at 675 kg, and an exceptionally heavy anchor, the Spek at 29 000 kg were included. Fig. 7 shows the modeled anchors and Table 4 summarizes the dimensions.

In terms of computational effort, the number of surfaces resulting from the geometry was kept low. Recesses of the anchors were omitted under the assumption that the structures opposite to the drag direction have little influence on the penetration behavior. Bulges and curves were replaced by edges in the models. Likewise, the anchor chain was greatly simplified geometrically according to Fig. 8.

The chain links are connected by hinges that allow twisting but prevent relative displacement. The chain is attached to the shank, and the shank to the fluke body, in the same way. Therefore, the anchor can adjust its opening angle which are limited between 0 and 35 ° or 40 °, as summarized in Table 4, to adapt to in-situ conditions.

The aspect ratios of the AC-14 anchor are the same for both the 675 kg anchor and the 8325 kg anchor. The corresponding dimensions can be found in Table 4. In each anchor model, the shank and anchor flukes are connected by hinges, which allow rotation according to Fig. 7.

Due to the low deformations compared to the soil, all anchor structures are modeled as rigid bodies.

3.4. Geometry of the soil domain and boundary conditions

To describe the soil, a Eulerian domain of size 100 m × 20 m × 6 m is created as depicted in Fig. 9. In the initial configuration, the lower 18 m are filled with soil, while the upper 2 m are modeled as void space to allow for any soil deformations in this region. Taking advantage of the existing symmetry, half of the real area is assumed for the calculation, so that the anchor can only move in the symmetry plane. At the reference point on the free chain link, the horizontal drag velocity v_i acts at the beginning of the drag phase. The distances between the boundary and the rigid structures were selected to ensure that, in the y-direction, at least 2.5 times $B/2$ (half of the anchor width) is maintained, and in the x-direction, at least 2.5 times the anchor length, including the chain length, is preserved. Passive wedges are expected to extend significantly in front of the anchor fluke. In lateral pile analysis, studies such as Al-Baghdadi et al. (2017) suggest lateral boundaries up to 60 times the pile diameter. In our study, lateral boundaries in x-direction directly in front of the anchor range from 15.5 to 56 times the anchor length. In addition to the minimum limits from preliminary investigations, we also considered the recommendations of Ullah et al. (2017), who evaluated boundary impacts from their physical tests and suggested limits between 2 and 5 times the structure width. In the preliminary investigations, no significant wave acceleration was observed at the model boundaries throughout the entire simulation. Therefore, the boundary space was considered sufficient. The entire domain is discretized into cuboidal Eulerian elements of type EC3D8R according to Fig. 10 and consists of a total of 256,166 elements.

Fig. 10 shows the boundary conditions for the Eulerian domain. The edges of the model section are unmovable and the upper edge of the seabed is exposed. For the anchor structures, the degrees of freedom in y-direction and the rotation around the x- and z-axis are suppressed.

3.5. Contact model for the anchor-seabed-interface

The interaction between Eulerian and Lagrangian materials is managed by a general contact approach based on the penalty contact method, as presented in Fig. 11. This algorithm introduces numerical softening through the implementation of penalty springs, but it does not explicitly enforce contact between Lagrangian and Eulerian elements. Therefore, Lagrangian elements can move through the Eulerian mesh freely until they encounter a Eulerian element filled with material (Eulerian volume fraction $\neq 0$). As this interaction occurs, seeds are activated on the edges and faces of Lagrangian elements and anchor points are established on the surface of the Eulerian material.

This penalty method offers an approximation of hard pressure-overclosure behavior, permitting slight penetration of the Eulerian material into the Lagrangian domain. The contact force, denoted as F, applied between seeds and anchor points, is proportional to the penetration distance x:

$$F = kx, \tag{5}$$

where k signifies the penalty stiffness, which is dependent on the properties of both the Lagrangian and Eulerian materials. No tensile stresses are transferred in this interaction. However, forces in the tangential to the anchor-soil-interface are propagated through a linear-elastic, ideal-plastic static-slip model, which considers Coulomb's friction law. For this, the wall friction coefficient μ is chosen with a value of $\tan\delta$. This model's underlying assumption is derived from the empirical value in the EAU (2020) that estimates the mobilized wall friction angle for the interaction between a rough steel surface and soil as $\delta = 2/3\varphi$.

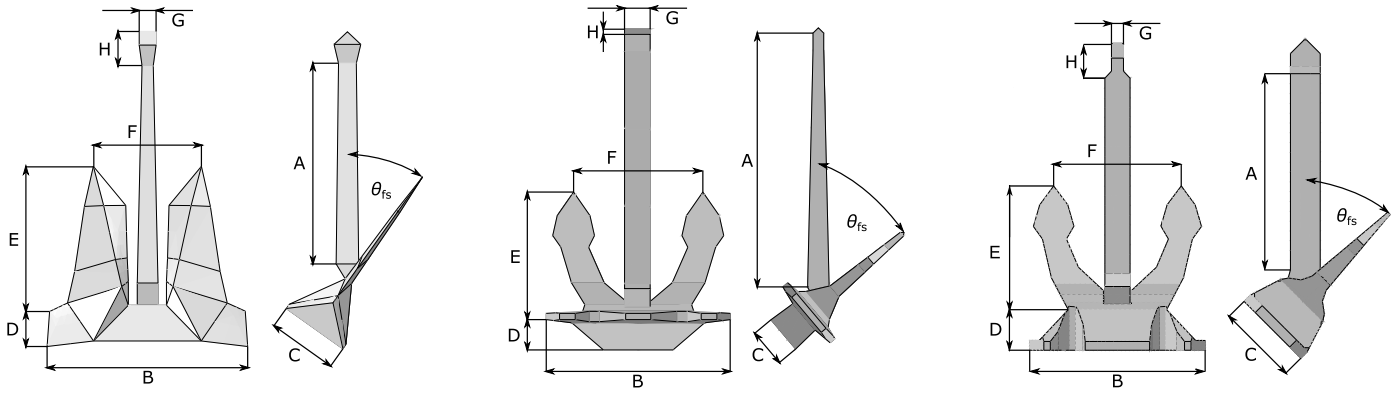

Fig. 7. Front and side views of the simplified AC-14 (left), Hall (middle) and Spek (right) anchor models.

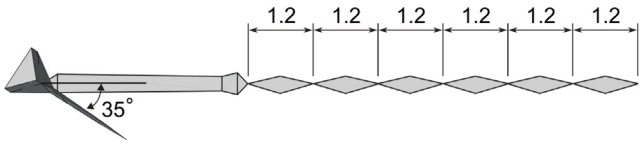

Fig. 8. Geometrically simplified anchor chain, exemplarily connected to an AC-14 anchor model (length dimensions in m).

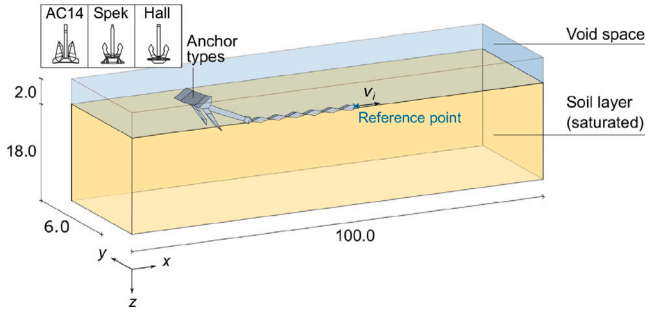

Fig. 9. Geometry of 3D model to simulate the penetration of an anchor in a homogeneous seabed (all dimensions in m).

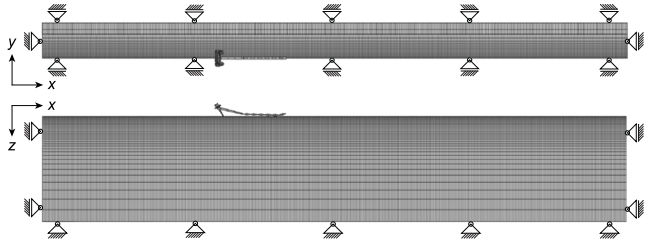

Fig. 10. Discretization of the model domain with Eulerian elements of type EC3D8R and its boundary conditions.

3.6. Load history and analysis procedure

Dynamic deformation analyses at fully drained conditions are performed to simulate the anchor penetration into the saturated seabed. At the beginning of the simulation, the earth pressure coefficient is assumed to be $K_0 = 0.5$. The constitutive parameters for the soil correspond to Table 3. The initial void ratio of $e_0 = 0.8, (I_d = 0.63)$ was chosen for the whole soil domain, which corresponds to the medium dense seabed that was found at the sample extraction location. The homogeneous void ratio distribution was adopted. The ship is simplified as a reference point with a horizontal velocity v_i, which pulls

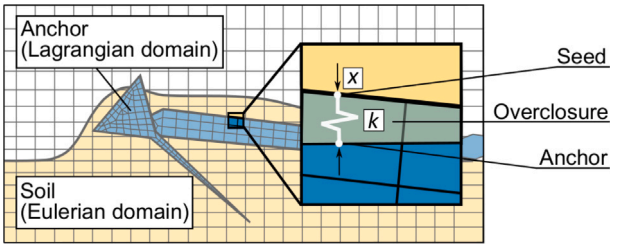

Fig. 11. Penalty contact algorithm.

the anchor and the chain. The reference point engages the free end of the chain, according to Fig. 9. At the beginning of the simulation, the anchor lies on the surface of the seabed. Here, the initial configuration corresponds to the results from simulations of drop tests of an AC-14 anchor in water (Grabe et al., 2015). In the second step, the restrictions in the z-direction are removed so that the anchor begins to penetrate the soil under its own weight. Then, the restrictions of the first chain link in the horizontal direction are deactivated and the velocity v_i is activated, starting the horizontal movement of the anchor. In the process, the anchor penetrates further forward into the seabed and causes stress on the soil. Consequently, the soil's resistance increases until further penetration is prevented, causing the anchor to resurface.

3.7. Validation of the numerical model

Fig. 12 compares the prediction of the numerical model for an 8.325 t AC-14 anchor in medium dense ($I_d = 0.63$) Baltic Sea sand of the current study with centrifuge test data for an 8.5 t AC-14 anchor at various relative densities of sand ($I_d = 0.82$, 0.55, and 0.38) by Sharif et al. (2023) under well-controlled conditions. The centrifuge tests demonstrate reduced penetration in denser sands.

The numerical model accurately replicates the sharp initial penetration observed in the centrifuge tests. As the anchor is dragged horizontally, the model shows a decrease in penetration depth, reflecting the increasing horizontal resistance of the sand, which aligns well with the centrifuge results. The overall shape and trend of the model's curve are close to those of the centrifuge tests, particularly for $I_d = 0.55$, also with a medium dense seabed. Throughout the range of horizontal displacements, the model's predicted penetration depth stays within the bounds of the centrifuge tests. The peak penetration depth in the model is lower than that in the $I_d = 0.82$ test and slightly higher than the $I_d = 0.55$ test, indicating that the penetration is consistent with the expected behavior for the specified density. Overall, the comparison reveals a strong correlation between the numerical model and the centrifuge test results. The model successfully captures key trends in anchor penetration and displacement, including the initial penetration

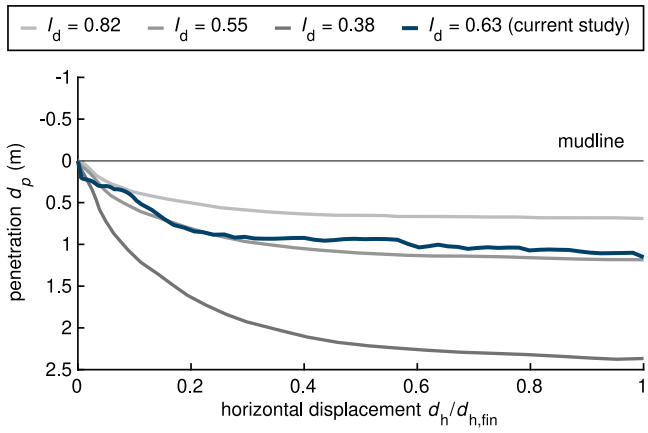

Fig. 12. Simulated penetration of the AC-14 anchor (8.375 t) compared to centrifuge tests with an AC-14 anchor (8.5 t) by Sharif et al. (2023) over the course of the horizontal displacement.

Table 5
Conducted drag phase simulations.

No.	Anchor type	m (t)	v_i (m/s)	$d_{h,fin}$ (m)
1	AC-14	0.675	1	12.5
2	AC-14	8.325	1	25.0
3	Hall	11.110	1	12.5
4	Spek	29.000	1	12.5
5	AC-14	0.675	3	12.5
6	AC-14	8.325	3	18.0
7	Hall	11.110	3	12.5
8	Spek	29.000	3	12.5

and subsequent reduction in depth observed in the centrifuge tests. This consistency demonstrates that the numerical model is reliable for predicting anchor behavior in sand.

4. Results and discussion

A series of eight simulations were executed under fixed drag velocities, which are summarized in Table 5. Two distinct velocities v_i were selected for the simulation to analyze inertial effects: 1 m/s and 3 m/s. The choice of 1 m/s, approximately equivalent to 2 kn, aligns with the commonly used velocity for the CBRA method (Trust, 2015a). On the other hand, 3 m/s, translating to roughly 6 kn, represents the upper threshold of realistic velocities for vessels. These selections ensure that our simulations encompass both standard and extreme operational conditions.

These simulations aim to mimic the penetration process of each anchor model into homogeneous Baltic Sea sand. Selected stages for each simulation are illustrated in Fig. 15.

In our analysis, we consider the penetration depth for horizontal displacements ranging from 0 to 25 m until a steady state of penetration is expected to be reached. The mudline is defined at $d_p = 0$. The penetration is negative when the anchor tip is above the seabed surface.

Additionally, we introduce the concept of stress circles to provide a visual representation of the altered stress state in the soil resulting from anchor penetration, offering a simplified representation of the changed stress.

4.1. Parametric study

The progression of the penetration depth for different anchors in Baltic Sea sand under different velocities is depicted in Fig. 13.

For AC-14 (8.375 t), at a velocity of v_i = 1 m/s, the anchor begins with a rapid penetration, followed by a more gradual increase in depth. In contrast, at v_i = 3 m/s, the penetration is shallower for the same horizontal displacement. AC-14 (0.675 t) exhibits a similar trend but initially resurfaces before penetrating the seabed, with deeper penetration at v_i = 1 m/s. The Hall anchor shows a steeper curve for v_i = 1 m/s and even resurfaces in the beginning for v_i = 3 m/s. The Spek anchor penetrates quickly at the start, with the growth in penetration depth decreasing over time, especially at v_i = 1 m/s. At v_i = 3 m/s, its penetration is relatively steady. A general trend across all anchors is an initial rapid penetration, slowing as horizontal displacement increases, and eventually approaching a plateau at maximum penetration depth due to increased soil resistance. This behavior aligns with expectations, considering initial soil disturbance and increasing soil resistance as the anchors move horizontally. Overall, the Spek anchor exhibited the most significant penetration depth under both velocities, followed by the 8.325 t AC-14, the Hall, and the 0.675 t AC-14 anchor from high to low penetration depth. Factors, such as velocity, weight, along with geometry, are influential in determining penetration capability.

4.1.1. Velocity impact

The AC-14 anchors show differences in penetration depths between the two velocities, with deeper penetration at the slower velocity. The Spek anchor shows less pronounced differences. Slower dragging speeds result in greater penetration depths, while higher speeds may result in the anchor gliding over the seabed, as shown in studies by Dao and Grabe (2022) and Grabe and Dao (2024). This observation is expected due to less dynamic impact at higher velocities to penetrate deeper before being dragged further. We assume that at higher velocities, the anchor's movement can impart more kinetic energy to the soil particles, potentially pushing them aside more easily than at slower velocities. The soil's resistance then becomes more a function of inertia and momentum rather than its mechanical properties at these higher velocities. A possible reason for this time-dependent behavior might be that the longer an anchor remains stationary or moves slowly, the more it can potentially penetrate vertically. At slower speeds or under stationary conditions, there could be a reduced dynamic impact, allowing a more consistent and deeper penetration as the soil below the anchor is compressed or moved aside gradually.

4.1.2. Weight impact

For further evaluation, Fig. 14 shows the calculated penetration depths for velocities v_i = 1 m/s and 3 m/s with the associated anchor mass and confirms previous findings from numerical and physical tests (Grabe et al., 2015; Dao and Grabe, 2022; Moore et al., 2021).

The efficiency of penetration, measured as depth per ton, varies among the anchors. Notably, the heavier AC-14 anchor, despite not being the heaviest, achieves a significant penetration depth relative to its weight, even penetrating deeper than the heavier Hall anchor. This finding underscores the fact that other factors, such as anchor shape, also play crucial roles in determining penetration depth.

The field tests by Luger and Harkes (2013) also maintain the same trend as the simulations regarding the anchor's mass efficiency. The exact magnitudes of penetration depth differ between the simulation and field tests, but performance of the AC-14 in the field tests was still efficient given its weight, indicating that it can achieve significant penetration with a moderate weight. The 11.1 t Hall anchor, despite being heavier than 8.325 t AC-14, did not demonstrate dramatically greater penetration depth either in simulation or field tests, nor did it achieve proportionally deeper penetration despite its greater weight.

4.1.3. Shape effects

The anchor's shape emerged as a significant determinant of penetration behavior. Pointed structures, such as anchor flukes, facilitated greater penetration into the soil, confirming findings from Dao and Dicke (2024). The influence of weight appeared to reduce for anchors above 8325 kg. For instance, the AC-14, with its narrow, sharply pointed flukes, achieved superior penetration depths compared to the

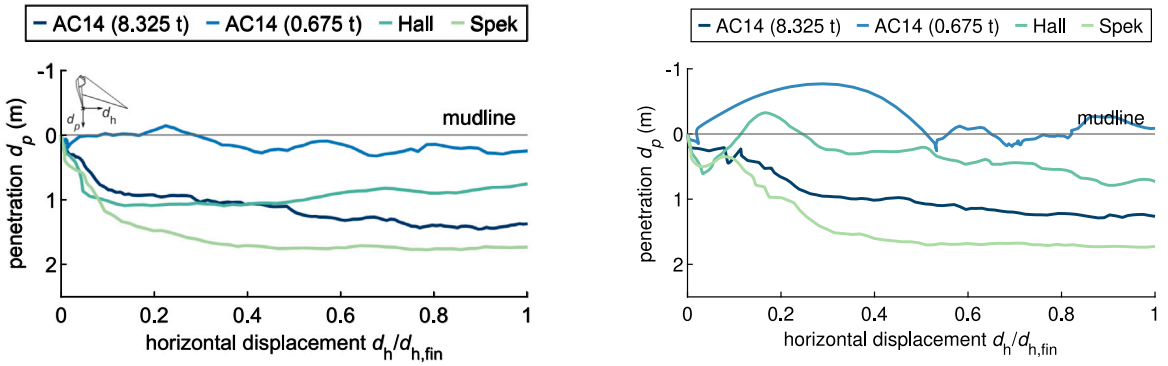

Fig. 13. Calculated penetration depth of different anchors at a drag velocity of v_i = 1 m/s (left) and v_i = 3 m/s (right) in homogeneous Baltic Sea sand.

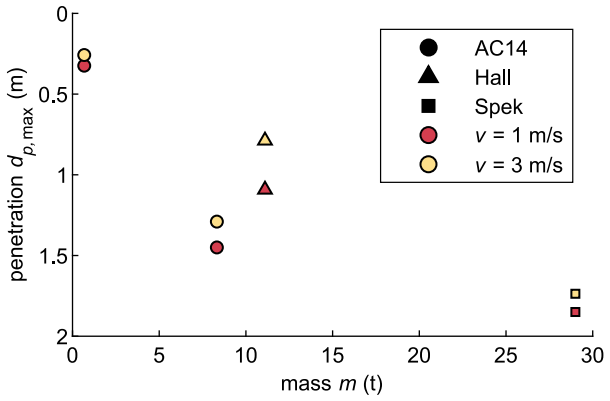

Fig. 14. Calculated maximum penetration depth of four anchors in homogeneous Baltic Sea sand at different velocities.

Hall anchor, despite its lighter mass. The Hall anchor's flukes are relatively blunter and shorter, limiting penetration. Fig. 16 shows the plate structure below the flukes (palms) of the Hall anchor highlighted in red. The larger plan surface area of approximately 1.6 m^2 perpendicular to drag direction causes soil to accumulate before moving sideways. This effect is more pronounced compared to the inclined surfaces of the AC-14 anchor with an area of about 1.2 m^2 when projected perpendicular to the drag direction. The flukes of the Spek anchor are also relatively blunt compared to those of the AC-14. However, the considerable mass difference between the 8325 kg AC-14 and the 29 t Spek anchor exert more influence on the penetration depth than that observed between the 8325 kg AC-14 and the 11.1 t Hall anchors.

In conclusion, the behavior of the anchors is significantly influenced by their design, weight, and the dragging velocity. The slower dragging velocity generally leads to deeper penetration across all anchors, but the rate and efficiency of penetration vary depending on the anchor type. The Spek anchor distinguishes itself in performance, achieving the greatest depth. The Spek's significant penetration at both velocities is consistent with its considerable weight, showing that the influence of weight is a significant factor, but not the sole determinant.

4.2. Stress circles

Generally, the resulting stress arch is complex. Fig. 17 shows an example for the normalized absolute maximum principal stress p, showing a cross-section of the soil and its stress state when the anchor fluke tip is at the maximum penetration depth $d_{p,max}$. Note that Fig. 17 is a snapshot of the stresses when the anchor is at its deepest point, focusing on the cross-section at the fluke tip and not representing the whole anchor nor the entire pulling phase. In the following analysis, We compare the stress exerted by the fluke tip. The anchor fluke is included for reference, while the shank is omitted for clarity. In the at-rest earth pressure state, Abaqus automatically groups the stress levels into 2-m layers, which we adopted, e.g.: 0 to 2 m as $\sigma_{ii,max,0}$, 2 to 4 m as $2\sigma_{ii,max,0}$ and so on. These stress groupings form the basis for representing stress distributions in the stress circles. Varying shades in Fig. 17 depict grouped areas of the normalized stress p. Therefore, p is a multiple of the initial level of the maximum principal stress at a depth of up to 2 m $\sigma_{ii,max,0}$.

Table 6
Stress depths $d_{s,i}$ of analyzed anchors.

Anchor type	$d_{p,max}$	$d_{s,2}$	$d_{s,3}$	$d_{s,4}$	$d_{s,5}$
AC-14 (0.675 t)	0.32	0.39	0.34	0.22	0.21
AC-14 (8.325 t)	1.45	1.93	1.73	1.68	1.61
Hall	1.09	1.42	1.26	1.18	1.15
Spek	1.85	2.35	2.12	2.03	1.93

$$p = \frac{|\sigma_{ii,max}|}{|\sigma_{ii,max,0}|} \tag{6}$$

The stress depths $d_{s,p}$ are defined as maximum distance between the mudline and the outline of the corresponding stress area around the fluke tip when an anchor has reached its greatest penetration depth $d_{p,max}$. In each simulation, $\sigma_{ii,max,0}$ was measured at the specified stress depths $d_{s,p}$ when the anchor fluke tip reached $d_{p,max}$.

While cable damage due to direct contact with ship anchors is evident, the implications of anchor-induced stresses extend beyond mere physical interactions. As shown in Osthoff et al. (2017), not only can direct contact with the anchor influence a cable, but the stresses introduced by the anchor into the soil can also indirectly impact the cable's integrity. Given the inherent challenges in measuring such induced stresses in situ, simulations offer a valuable alternative for assessing these interactions. Here, the extent of different stress levels, measured from the top of the undisturbed seabed according to Fig. 17, are summarized in Table 6.

A simplified representation of the stress field as stress sphere or stress circle is introduced. The radii $r_{s,i}$ are calculated, according to Eq. (7).

$$r_{s,p} = d_{s,p} - d_{p,\,max} \tag{7}$$

The stress depth $d_{s,p}$ is determined according to Fig. 17 and is extracted from Abaqus. An example 3D representation is shown for a half anchor in Fig. 18. Each anchor presents its unique stress distribution, with weight and geometry playing a crucial role in the stress sphere's size. The size and spread of the circles give insights into the depth and reach of an anchor's influence. For instance, a larger circle for a specific anchor denotes that its stress influence penetrates further into the soil compared to an anchor exhibiting a smaller circle at the same stress level. This offers an intuitive way to compare how different anchors

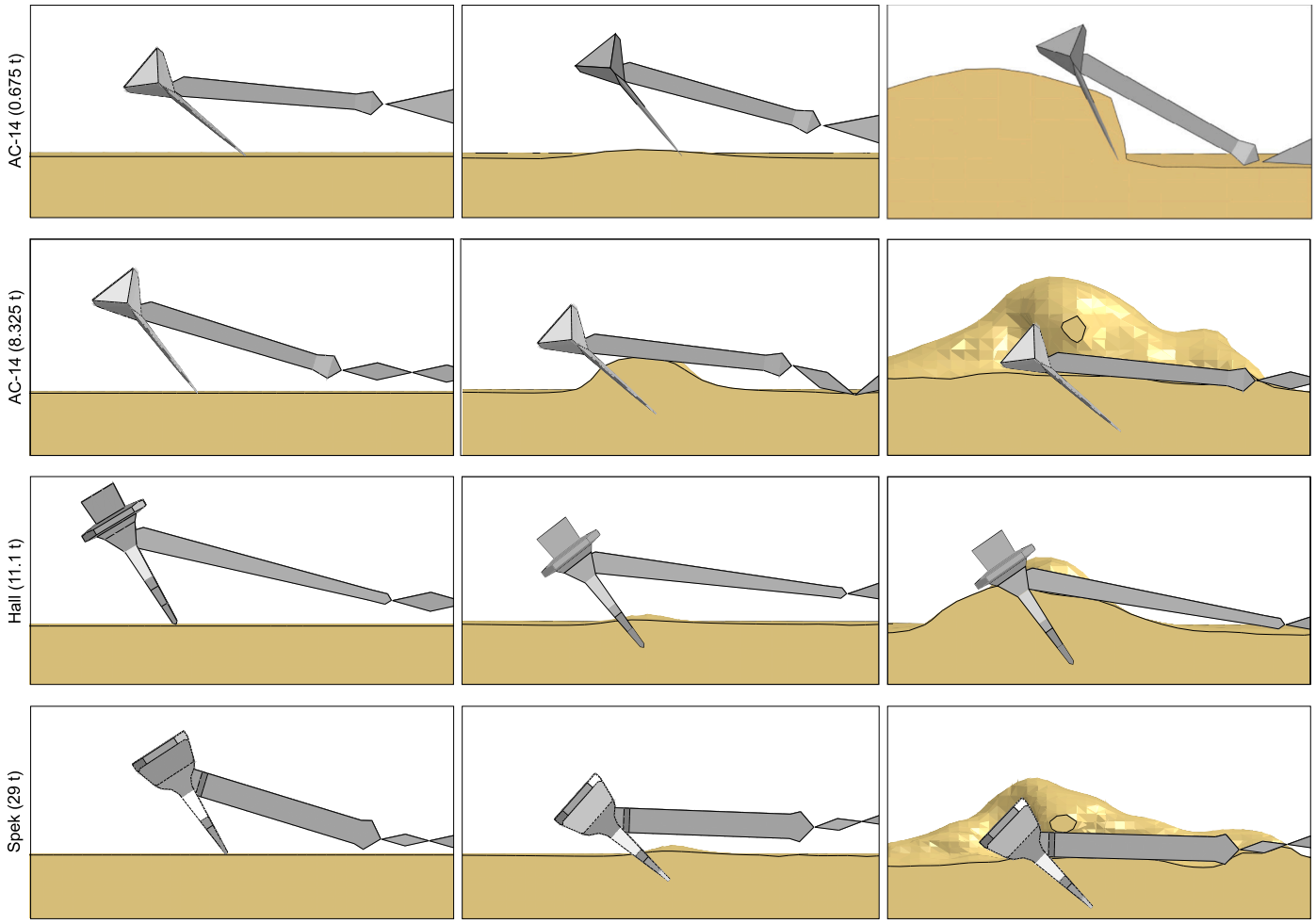

Fig. 15. Selected phases of the penetration process for different anchor types at a drag velocity of $v_i = 1$ m/s in homogeneous sand.

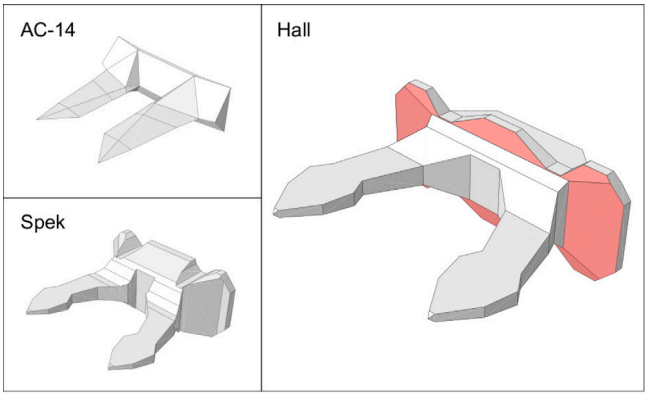

Fig. 16. Non-scale comparison of the fluke shapes of the AC-14 (left, top), Spek (left, bottom) and Hall (right) anchors shown without shank.

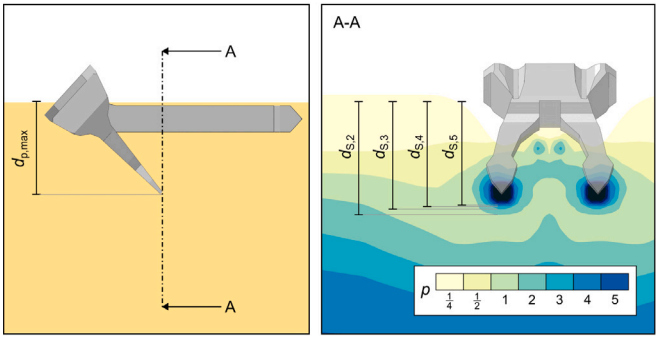

Fig. 17. Definition of the penetration depth when reaching its maximum $d_{p,max}$ (left) and the resulting stress arches (of the normalized absolute maximum principal stress p) with corresponding depths $d_{s,p}$ (right).

influence soil at various stress levels and depths. Note that the actual shape of the stress field in real scenarios is considerably more complex than the representations used in this study. In reality, the stresses experienced on the side of the flukes not facing the direction of drag are expected to be significantly lower. The stress circle approach presents a simplified circular distribution. It does not account for detailed localization or the upward stress concentration associated with passive wedge formation, as demonstrated in pipeline plough studies using PIV by Dingle et al. (2008) and White and Dingle (2011), or as discussed by White and Cathie (2010) and Neubecker and Randolph (1996b). The chosen spherical shape of the stress circles, though beneficial for visualizing and understanding the magnitude and general distribution of stress, is therefore a conservative approximation.

Fig. 19 shows a comprehensive visual representation in 2D using stress circle plots for the four anchor types analyzed. Each anchor type is provided its subplot, allowing individual analysis and comparison.

The plots essentially represent the spatial extent of stress fields (or stress spheres) exerted by the anchor's fluke tip R_P in the surrounding soil. R_P is represented by a black point at the center of each subplot,

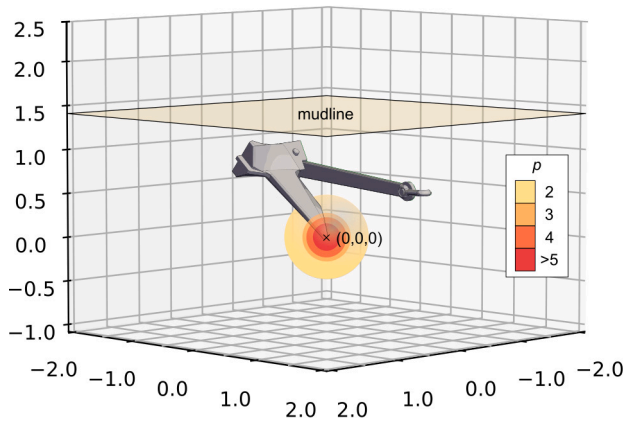

Fig. 18. Three-dimensional representation of the simplified stress field as stress sphere for an AC-14 anchor half at its maximum penetration depth $d_{p,\ max}$.

serving as the originating point from which the stress circles radiate outwards. The mudline in each subplot represents the undisturbed surface of the seabed. The point of application of a load will induce stresses in the surrounding material, with stresses dissipating as we move away from the load point. As we move further from the source, the stress influence diminishes. Therefore, the concentric rings surrounding the fluke tip denote varying levels of stress with the outermost ring representing the least stress, and each inner ring representing progressively higher stress levels. A larger circle overall implies a more extensive stress distribution. The normalization of the stress is achieved by dividing by the maximum initial stress level $|\sigma_{ii,max,0}|$ of 16.67 kPa that is present up until 2 m embedment depth. Furthermore, the circles are distinguished by different shades, each representing a particular normalized stress.

The AC-14 (8.325 t) showcases the largest stress sphere among the four, with a wider and deeper influence. Given its substantial weight, this is expected. It implies the largest area of disturbance when penetrating the soil. Despite the same design as its heavier version, the much lighter weight of the AC-14 (0.675 t) results in a drastically smaller stress sphere, emphasizing the significant role of weight in stress distribution. Furthermore, the smaller AC-14 anchor exhibits a distinctive behavior where, under the same conditions, it does not form its maximum stress sphere at the tip of the fluke, but rather slightly above it, at a higher edge that penetrates the ground earlier, see Table 6. For the illustration of the stress circles, the tip of the fluke for the AC-14 was therefore shifted to the center of the stress circle to accommodate this anomaly. The Hall anchor exhibits a moderate-sized stress sphere. The Spek anchor displays a stress circle comparable to the Hall anchor but with a slightly deeper influence. A heavier anchor's deeper penetration can result in larger stress spheres. Additionally, it can induce higher stresses in the soil, leading to a pronounced stress distribution. Sharp flukes like the ones from the AC-14 anchor penetrate more efficiently, influencing the stress spheres's extent. Broad flukes lead to shallower penetration.

The stress circles identified in this study showcase the zones of soil disturbance that extend beyond the direct path of anchor penetration. The stress induced by the anchor could compromise the soil integrity in these zones.

For typical sea cables, such as AC or DC, the maximum tensile stresses in the elastic range are between 50 000 and 55 000 kN/m^2 (Ehlers et al., 2023). The stresses occurring up to the stress ring $n = 4$ are thus well below the limit. For $n \geq 5$, the corresponding circles show diameters around the maximum penetration depth $d_{p,\ max}$ that do not exceed 0.16 m. Thus, the extension of these high stresses are already included in the safety margins when determining the minimum burial depth by existing standards.

5. Conclusions

The results from the simulations of high-speed emergency deployment and subsequent anchor drag lead to several key conclusions: The drag velocity of anchors was determined to have a significant influence on their penetration depth. For instance, slower drag velocities consistently resulted in deeper anchor penetrations, while higher velocities often yielded shallower penetration due to potential gliding over the seabed. These installation rate effects on penetration are due to anchor inertial effects only, as neither viscous nor drainage effects were considered.

Anchor weight emerged as a pivotal factor influencing penetration depth. As observed, heavier anchors, due to their increased downward force, generally achieved greater penetration depths. However, when considering penetration efficiency, quantified as depth per unit weight, there were variations among the anchors. For example, the AC-14 (8.325 t) anchor achieved deeper penetration relative to its weight compared to the heavier 11.1 t Hall anchor due to shape effects.

The size and design of the anchor, particularly the configuration of its flukes, played a crucial role in impacting penetration depths. Anchors designed with pointed structures achieved greater penetration into the seabed than those with broader or blunter designs with larger surface areas perpendicular to drag direction.

The introduction of stress circles provide a practical, simplified visualization of the spatial stress distribution exerted by the anchor's fluke tip within the seabed. The size of these circles are correlated with the depth and breadth of the anchor's influence, with larger circles indicating a more profound effect. Additionally, the outer rings of the stress sphere, which represent areas of lower stress, suggest

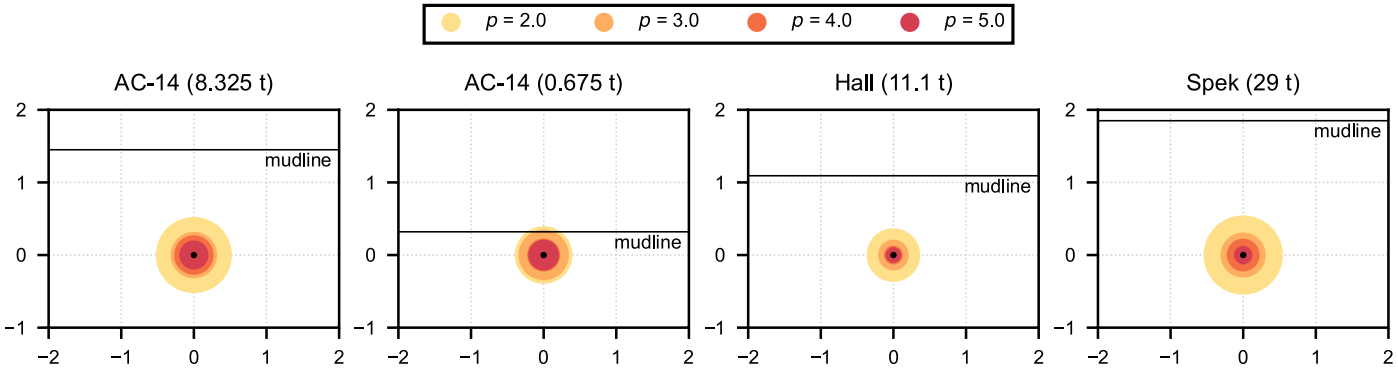

Fig. 19. Stress circles of various ship anchors at their maximum penetration depths $d_{p,\ max}$ in Baltic Sea sand.

minimal potential damage to robust subsea installations like cables. The material of these cables is generally resilient enough to withstand the additional stresses from anchor penetration, especially those from the outer regions of the stress spheres. Consequently, direct harm leading to significant damage is not anticipated.

Considering the implications for subsea installations, the research indicates that understanding both the penetration depth and the stress distribution of anchors is essential for determining safe burial depths, particularly for subsea cables in the Baltic Sea. The stress circles highlight areas of soil disturbance beyond the direct path of anchor penetration, suggesting optimal protection is achieved when subsea installations are buried beyond the furthest extent of these stress spheres. As previously discussed, the simplified stress spheres do not capture localization or passive wedge formation resulting from the predominant upward stress concentration above the anchor rather than below the fluke tip. Thus, these spheres only provide an indication of the average stress regime. The primary risk still arises when the cable is located directly in front of the anchor.

In summary, this study underscores the complex relations between anchor design, weight, and drag velocity in determining both penetration depth and stress distribution within the seabed. Based on these findings, stakeholders involved in subsea cable installations in the Baltic Sea, or similar maritime regions, should take a comprehensive approach, considering both direct anchor penetrations and broader soil disturbances, to determine optimal burial depths. This ensures not only the physical protection of the cables but also the continuity of their operational efficacy.

6. Notation list

The following symbols are used in this paper:

C	Compression index;
c_d	Dilatory wave velocity (m/s);
D	Deformation rate tensor;
d_p	Anchor penetration depth (m);
$d_{p,\max}$	Maximum penetration depth (m);
$d_{s,p}$	Stress depth (m);
d_h	Drag distance (m);
$d_\mathrm{h,fin}$	Final drag distance (m);
E	Young's modulus (kN/m^2);
E_s	Modulus of elasticity (kN/m^2);
e	Void ratio;
e_0	Initial void ratio;
e_c	Limiting critical void ratio;
e_c0	Critical state void ratio at zero pressure;
e_d	Limiting minimum void ratio;
e_d0	Minimum void ratio at zero pressure;
e_i	Limiting maximum void ratio;
e_i0	Maximum void ratio at zero pressure;
e_max	Maximum void ratio;
e_min	Minimum void ratio;
F	Contact force (kN);
h_s	Granulate hardness (MPa);
I_d	Relative density;
K_0	Earth pressure coefficient at rest;
k	Penalty stiffness (kN/m);
L	Characteristic element length (m);
$\mathcal{M}$	Fourth-order stiffness tensor;
m	Mass (kg);
m_R	Stiffness increase factor;
T	Stress tensor;
m_T	Stiffness increase factor;
n	Pressure-sensitivity exponent;
p	Normalized absolute maximum principal stress;
p_s	Pressure (kN/m^2);
R_max	Maximum intergranular strain;
R_p	Anchor fluke tip;
$r_{s,i}$	Stress circle radius (m);
$\overset{\circ}{\mathrm{T}}$	Stress rate tensor;
U	Uniformity coefficient;
v_i	Horizontal drag velocity (m/s).
x	Penetration distance (m);
α	Exponent for density dependence of the peak friction angle;
β	Exponent for density dependence of the stiffness modulus;
β_χ	Exponent for intergranular strain development;
Δt_crit	Critical time step size (s);
δ	Mobilized wall friction angle (°);
ε	Strain (%);
θ_fs	Fluke-shank angle (°);
μ	Wall friction coefficient;
ρ	Density (kg/m^3);
$\sigma_{ii,\max}$	Maximum principal stress (kN/m^2);
$\sigma_{ii,\max,0}$	Initial maximum principal stress (kN/m^2);
σ_v	Vertical stress (kN/m^2);
φ_c	Critical state friction angle (°);
φ_p	Peak friction angle (°);
χ	Stiffness degradation exponent;

CRediT authorship contribution statement

D.A. Dao: Writing – original draft, Visualization, Software, Investigation, Formal analysis, Data curation. **J. Grabe:** Writing – review & editing, Writing – original draft, Validation, Supervision, Software, Resources, Project administration, Methodology, Investigation, Funding acquisition, Formal analysis, Data curation, Conceptualization.

Declaration of competing interest

The authors declare the following financial interests/personal relationships which may be considered as potential competing interests: Duy Anh Dao reports financial support was provided by 50Hertz Transmission GmbH. If there are other authors, they declare that they have no known competing financial interests or personal relationships that could have appeared to influence the work reported in this paper.

Acknowledgments

We thank 50Hertz Transmission GmbH for the provision of soil samples of Baltic Sea sand. Furthermore we thank our students Scarlett Maeve Minshull and Noah Mathew Hector Coutinho for providing graphical assistance.

Data availability

Some or all data, models, or code that support the findings of this study are available from the corresponding author upon reasonable request.

References

50Hertz Transmission GmbH, 2024. Offshore projects - grid development. URL https://www.50hertz.com/en/Grid/Griddevelopement/Offshoreprojects. (Accessed 09 August 2024).

Al-Baghdadi, T.A., Brown, M.J., Knappett, J.A., Al-Defae, A.H., 2017. Effects of vertical loading on lateral screw pile performance. Proc. Inst. Civ. Eng. - Geotech. Eng. 170 (3), 259–272. http://dx.doi.org/10.1680/jgeen.16.00114.

Allan, P., 1999. Selecting appropriate cable burial depths – a methodology. In: Submarine Communications.

American Bureau of Shipping, 2018. Guidance Notes - Design and Installation of Drag Anchors and Plate Anchors. American Bureau of Shipping.

Andresen, A., Berre, T., Kleven, A., Lunne, T., 1979. Procedures used to obtain soil parameters for foundation engineering in the North Sea. Mar. Geotechnol. 3 (3), 201–266. http://dx.doi.org/10.1080/10641197909379804.

Atkinson, J., 2017. The Mechanics of Soils and Foundations. CRC Press.

Attwood, J.R., 2000. Cable design for subsea power links. IEEE Power Eng. Rev. 20 (9), 13–14. http://dx.doi.org/10.1109/39.866861.

Aubeny, C.P., Chi, C., 2010. Mechanics of drag embedment anchors in a soft seabed. J. Geotech. Geoenviron. Eng. 136 (1), 57–68.

Aubeny, C.P., Gilbert, R., Randall, R., Zimmerman, E., McCarthy, K., Chen, C.-H., Drake, A., Yeh, P., Chi, C.-M., Beemer, R., 2011. The Performance of Drag Embedment Anchors (DEA). Texas A&M University.

Bauer, E., 1996. Calibration of a comprehensive hypoplastic model for granular materials. Soils Found. 36 (1), 13–26.

BAW, 2012. Bericht zur Vermessung der Ankereindringtiefe: Untersuchung des Eindringverhaltens von Schiffsankern mittels Ankerzugversuchen.

Bienen, B., Fan, S., Schröder, M., Randolph, M.F., 2021. Effect of the installation process on monopile lateral response. Proc. Inst. Civ. Eng.-Geotech. Eng. 174 (5), 530–548, https://doi.org/10.1680/jgeen.20.00219.

Bjerrum, L., 1973. Geotechnical problems involved in foundations of structures in the North Sea. Géotechnique 23 (3), 319–358.

BSH, 2020. Environmental report on the site development plan 2020 for the German Baltic Sea. BSH number 7608.

Byrne, T., Gavin, K., Prendergast, L., Cachim, P., Doherty, P., Chenicheri Pulukul, S., 2018. Performance of CPT-based methods to assess monopile driveability in North Sea sands. Ocean Eng. 166, 76–91. http://dx.doi.org/10.1016/j.oceaneng.2018.08.010.

Dahlberg, R., 1998. Design Procedures for Deepwater Anchors in Clay. In: Offshore Technology Conference. OTC, Houston, Texas, pp. OTC–8837–MS. http://dx.doi.org/10.4043/8837-MS.

Dao, D.A., Alkateeb, D., Schröder, M., 2023. Discrepancies between element tests and large-scale LDFE simulations: A case study on anchor kinematics during installation in clay. Comput. Geotech. 163, 105698. http://dx.doi.org/10.1016/j.compgeo.2023.105698.

Dao, D.A., Banduch, M., 2023. Geotechnical laboratory investigation on the Baltic Sea sand sample Z_VC_011. http://dx.doi.org/10.15480/882.8440.

Dao, D.A., Dicke, K., 2024. Numerical investigation of drag embedment anchor model reduction for FOWTs in coarse and fine-grained Baltic Sea soil. In: Proceedings of 5th International Conference on Geotechnics for Sustainable Infrastructure Development (Geotec Hanoi 2023) in Hanoi, Vietnam. pp. 2871–2886. http://dx.doi.org/10.1007/978-981-99-9722-0_199.

Dao, D.A., Dicke, K., Grabe, J., 2022. Investigation of anchor installation for floating offshore wind turbines. In: Proceedings of 10th International Conference on Physical Modelling in Geotechnics (ICPMG 2022) in Daejon, Korea. pp. 482–485.

Dao, D.A., Grabe, J., 2022. Numerical investigation of ship anchor penetration in cohesive Baltic Sea soil. In: 41st International Conference on Ocean, Offshore and Arctic Engineering (OMAE 2022) in Germany, Hamburg. Volume 9: Offshore Geotechnics, V009T10A002. http://dx.doi.org/10.1115/OMAE2022-80822.

Dao, D.A., Grabe, J., Chmelnizkij, A., 2024. Examination of an analytical approach for load-displacement behavior of drag embedment anchors and their geometrical optimization. In: 43rd International Conference on Ocean, Offshore and Arctic Engineering (OMAE 2024) in Singapore. American Society of Mechanical Engineers, V008T10A011. http://dx.doi.org/10.1115/omae2024-124377.

Dassault Systèmes, 2018. Abaqus user's manual, version 6.18.

de Kuiter, J., Beringen, F.L., 1979. Pile foundations for large North Sea structures. Mar. Geotechnol. 3 (3), 267–314. http://dx.doi.org/10.1080/10641197909379805.

DIN 14688-2, 2020. Geotechnical investigation and testing - Identification and classification of soil - Part 2: Principles for a classification (ISO 14688-2:2017). Deutsches Institut für Normung, Beuth Verlag, Berlin.

DIN 18126, 2022. Soil, investigation and testing - Determination of density of non cohesive soils for maximum and minimum compactness. Deutsches Institut für Normung, Beuth Verlag, Berlin.

Dingle, H., White, D., Gaudin, C., 2008. Mechanisms of pipe embedment and lateral breakout on soft clay. Can. Geotech. J. 45 (5), 636–652. http://dx.doi.org/10.1139/t08-009.

Dinmohammadi, F., Flynn, D., Bailey, C., Pecht, M., Yin, C., Rajaguru, P., Robu, V., 2019. Predicting damage and life expectancy of subsea power cables in offshore renewable energy applications. IEEE Access 7, 54658–54669. http://dx.doi.org/10.1109/access.2019.2911260.

DNV, 2021. Subsea power cables for wind power plants. DNV-ST-0359.

EAU, 2020. Empfehlungen des Arbeitsausschusses "Ufereinfassungen" häfen und Wasserstraßen EAU 2020.

Ehlers, S., Biglu, M., von Bock und Polach, F., Thießen, W., 2023. Experimental and numerical investigations of the ultimate strength of two subsea power-transmission cables. Mar. Struct. 88, 103346. http://dx.doi.org/10.1016/j.marstruc.2022.103346.

Gao, P., Duan, M., Gao, Q., Jia, X., Huang, J., 2016. A prediction method for anchor penetration depth in clays. Ships Offshore Struct. 11 (7), 782–789. http://dx.doi.org/10.1080/17445302.2015.1116244.

Giampa, J.R., Bradshaw, A.S., 2018. A simple method for assessing the peak friction angle of sand at very low confining pressures. Geotech. Test. J. 41 (4), 639–647. http://dx.doi.org/10.1520/GTJ20170134.

Grabe, J., Dao, D.A., 2024. Modeling the interaction between ship anchors and cables in baltic sea soils. In: Proceedings of the 17th Pan-American Conference on Soil Mechanics and Geotechnical Engineering, la Serena, Chile.

Grabe, J., Qiu, G., Wu, L., 2015. Numerical simulation of the penetration process of ship anchors in sand. Geotechnik 38 (1), 36–45. http://dx.doi.org/10.1002/gete.201400022.

Grabe, J., Wu, L., 2016. Coupled Eulerian-Lagrangian simulation of the penetration and braking behaviour of ship anchors in clay. Geotechnik 39 (3), 168–174. http://dx.doi.org/10.1002/gete.201500028.

Herle, I., Gudehus, G., 1999. Determination of parameters of a hypoplastic constitutive model from properties of grain assemblies. Mech. Cohes. Frict. Mater. 4 (5), 461–486. http://dx.doi.org/10.1002/(SICI)1099-1484(199909)4:5<461::AID-CFM71>3.0.CO;2-P.

Hutchison, Z.L., Gill, A.B., Sigray, P., He, H., King, J.W., 2021. A modelling evaluation of electromagnetic fields emitted by buried subsea power cables and encountered by marine animals: Considerations for marine renewable energy development. Renew. Energy 177, 72–81. http://dx.doi.org/10.1016/j.renene.2021.05.041.

Jensen, M.R., Kellezi, L., 2023. Geotechnical characteristics of siliceous North Sea sands. Can. Geotech. J. 60 (10), 1545–1556.

Jongergouw, M., 2001. Industry developments in burial assessment surveying. In: SubOptic 2001.

Jostad, H.P., Dahl, B.M., Page, A., Sivasithamparam, N., Sturm, H., 2020. Evaluation of soil models for improved design of offshore wind turbine foundations in dense sand. Géotechnique 70 (8), 682–699. http://dx.doi.org/10.1680/jgeot.19.TI.034.

Lee, S.-W., Sasa, K., Chen, C., Waskito, K.T., Cho, I.-S., 2022. Novel safety evaluation technique for ships in offshore anchorage under rough seas conditions for optimal ship routing. Ocean Eng. 253, 111323. http://dx.doi.org/10.1016/j.oceaneng.2022.111323.

Luger, D., Harkes, M., 2013. Anchor Tests German Bright. Technical Report, Deltares.

Lux, J., Olschewski, M., Schäfer, P., Hill, W., 2019. Real-time determination of depth of burial profiles for submarine power cables. IEEE Trans. Power Deliv. 34 (3), 1079–1086. http://dx.doi.org/10.1109/TPWRD.2018.2881770.

Maitra, S., Tian, Y., Cassidy, M.J., 2022. Investigation of the installation process of drag-in plate anchors from LDFE modelling. Géotechnique 1–13. http://dx.doi.org/10.1680/jgeot.21.00402.

Mole, P., Featherstone, J., Winter, S., 1997. Cable protection – solutions through new installation and burial approaches. In: SubOptic 1997.

Moore, E., Haigh, S.K., Eichhorn, G.N., 2021. Anchor penetration depth in sandy soils and its implications for cable burial. Ocean Eng. 235, 109411. http://dx.doi.org/10.1016/j.oceaneng.2021.109411.

Murff, J.D., 1994. Limit analysis of multi-footing foundation systems. In: Proceedings of the 8th International Conference on Computer Methods and Advances in Geomechanics. Vol. 1, pp. 223–244.

Naval Civil Engineering Laboratory, 1982. Drag Embedment Anchor Tests in Sand and Mud - NCEL Techdata Sheet. Technical Report, Naval Civil Engineering Laboratory, URL https://apps.dtic.mil/sti/citations/ADB068224.

Neubecker, S., Randolph, M., 1996a. The performance of drag anchor and chain systems in cohesive soil. Mar. Georesour. Geotechnol. 14 (2), 77–96. http://dx.doi.org/10.1080/10641199609388305.

Neubecker, S.R., Randolph, M.F., 1996b. The kinematic behaviour of drag anchors in sand. Can. Geotech. J. 33 (4), 584–594. http://dx.doi.org/10.1139/t96-084-306.

Neubecker, S.R., Randolph, M.F., 1996c. The static equilibrium of drag anchors in sand. Can. Geotech. J. 33 (4), 574–583. http://dx.doi.org/10.1139/t96-083-305.

Niemunis, A., Herle, I., 1997. Hypoplastic model for cohesionless soils with elastic strain range. Mech. Cohes.-Frict. Mater.: Int. J. Exp. Model. Comput. Mater. Struct. 2 (4), 279–299.

O'Neill, M.P., Bransby, M.F., Randolph, M.F., 2003. Drag anchor fluke soil interaction in clays. Can. Geotech. J. 40 (1), 78–94.

O'Neill, M., Randolph, M., 2001. Modelling drag anchors in a drum centrifuge. Int. J. Phys. Model. Geotech. 1 (2), 29–41. http://dx.doi.org/10.1680/ijpmg.2001.010203.

O'Shaughnessy, E., Heeter, J., Shah, C., Koebrich, S., 2021. Corporate acceleration of the renewable energy transition and implications for electric grids. Renew. Sustain. Energy Rev. 146, 111160. http://dx.doi.org/10.1016/j.rser.2021.111160.

Osthoff, D., Heins, E., Grabe, J., 2017. Impact on submarine cables due to ship anchor - soil interaction. Geotechnik 40 (4), 265–270. http://dx.doi.org/10.1002/gete.201600027.

Peccin Da Silva, A., 2021. Macro-element modelling of plate anchors for floating offshore structures accounting for capacity changes during operational conditions (Ph.D. thesis). University of Bristol.

Randolph, M., Gourvenec, S., 2017. Offshore Geotechnical Engineering. CRC Press.

Santamarina, J.C., Cho, G.C., 2001. Determination of critical state parameters in sandy soils—Simple procedure. Geotech. Test. J. 24 (2), 185–192. http://dx.doi.org/10.1520/GTJ11338J.

Sharif, Y., Brown, M., Coombs, W.M., Augarde, C., Bird, R., Carter, G., Macdonald, C., Johnson, K., 2023. Characterization of anchor penetration behaviour for cable burial risk assessment. In: 9th International SUT OSIG Conference "Innovative Geotechnologies for Energy Transition". pp. 555–562.

SoilModels.com, 2024. Hypoplastic sand model with intergranular strain. URL https://soilmodels.com/hyposand/. (Accessed 09 August 2024).

Stapelfeldt, M., Alkateeb, D., Grabe, J., Bienen, B., 2020. Numerical simulation of cone penetration tests inside suction caisson foundations in sand. In: International Conference on Offshore Mechanics and Arctic Engineering. Vol. 84423, American Society of Mechanical Engineers, V010T10A007.

Thorne, C.P., 1998. Penetration and load capacity of marine drag anchors in soft clay. J. Geotech. Geoenviron. Eng. 124 (10), http://dx.doi.org/10.1061/(ASCE)1090-0241(1998)124:10(945).

Trust, C., 2015a. Application Guide for the specification of the Depth of Lowering using the Cable Burial Risk Assessment (CBRA) Methodology. Technical Report, Carbon Trust.

Trust, C., 2015b. Cable Burial Risk Assessment Methodology Guidance for the Preparation of Cable Burial Depth of Lowering Specification. Technical Report, Carbon Trust.

Ullah, S.N., Hu, Y., Stanier, S., White, D., 2017. Lateral boundary effects in centrifuge foundation tests. Int. J. Phys. Model. Geotech. 17 (3), 144–160. http://dx.doi.org/10.1680/jphmg.15.00034.

von Wolffersdorff, P.-A., 1996. A hypoplastic relation for granular materials with a predefined limit state surface. Mech. Cohes.-Frict. Mater.: Int. J. Exp. Model. Comput. Mater. Struct. 1 (3), 251–271.

Vryhof Anchors, 2018. Vryhof Anchors - Anchor manual 2018. URL https://vryhof.com/anchor-manual/. (Accessed 09 August 2024).

Watson, S.J., Ribó, M., Seabrook, S., Strachan, L.J., Hale, R., Lamarche, G., 2022. The footprint of ship anchoring on the seafloor. Sci. Rep. 12 (1), http://dx.doi.org/10.1038/s41598-022-11627-5.

White, D., Cathie, D., 2010. Geotechnics for subsea pipeline. Front. Offshore Geotech. II http://dx.doi.org/10.1201/b10132-6.

White, D., Dingle, H., 2011. The mechanism of steady friction between seabed pipelines and clay soils. Géotechnique 61 (12), 1035–1041. http://dx.doi.org/10.1680/geot.8.t.036.

Zhu, X., Hao, Q., Zhang, J., 2019. Buried depth of a submarine pipeline based on anchor penetration. J. Mar. Sci. Eng. 7 (8), 257. http://dx.doi.org/10.3390/jmse7080257.